Proceedings of the ASME 2019 Heat Transfer Summer Conference
HT2019
July 14-17, 2019, Bellevue, WA, USA

HT2019-3512

COMPARISON OF MODEL PREDICTIONS AND PERFORMANCE TEST DATA FOR A PROTOTYPE THERMAL ENERGY STORAGE MODULE

Dre Helmns[1], **Van P. Carey**[1], **Navin Kumar**[2], **Debjyoti Banerjee**[2], **Arun Muley**[3], and **Michael Stoia**[3]

[1]Mechanical Engineering Department, University of California, Berkeley, California 94709
[2]Mechanical Engineering Department, Texas A&M University, College Station, Texas 77843
[3]Boeing Research & Technology, The Boeing Company, Huntington Beach, California 92647

ABSTRACT

Although model predictions of thermal energy storage (TES) performance have been explored in several previous investigations, information that allows experimental validation of performance models has been very limited. This is particularly true for high-performance TES designs that facilitate fast input and extraction of energy. In this paper, we present a summary of performance tests of a high-performance TES unit using lithium nitrate trihydrate phase change material (PCM) as a storage medium. Our experimental program also included thorough property determinations and cyclic testing of the PCM. Performance data is presented for complete dual-mode cycles consisting of extraction (melting) followed by charging (freezing). These tests simulate the daylong cyclic operation of a TES unit for asynchronous cooling in a power plant. The model analysis is found to agree very well, within 10%, with the experimental data except for conditions very near the initiation of freezing. Slight deviation from the predicted performance at that time is a consequence of subcooling that is required to initiate solidification. The comparisons presented here demonstrate the viability of thermal energy storage for augmentation of power plant air-cooled condensers as well as other potential applications.

NOMENCLATURE

A_c	Cross sectional area of the working fluid flow passage.
$c_{p,s}$	Effective specific heat of the storage matrix.
$c_{p,w}$	Specific heat of the working fluid.
h_{ls}	Latent heat of fusion of the PCM in the storage matrix.
k_s	Effective thermal conductivity of the storage matrix.
k_w	Thermal conductivity of the working fluid.
L	Length of the TES device.
$\dot{m}$	Working fluid mass flow rate per passage.
s_w	Wetted perimeter of the working fluid flow passage.
T_e	Temperature of a discrete element in the storage matrix.
T_m	Melt temperature of the PCM in the storage matrix.
T_{max}	Maximum temperature encountered in the TES device.
T_{min}	Minimum temperature encountered in the TES device.
T_w	Temperature of a discrete parcel of working fluid.
U	Overall heat transfer coefficient.
x_e	Melt fraction of a discrete element in the storage matrix.
Δt^*	Non-dimensional temporal discretization.
$\Delta\hat{z}$	Non-dimensional spatial discretization.
ε_s	Fraction of the storage matrix occupied by PCM.
θ	Dimensionless temperature of a discrete element in the storage matrix.
ν'	Storage matrix volume per unit length of the device.
ρ_s	Effective density of the storage matrix.
ρ_w	Density of the working fluid.
ϕ	Dimensionless temperature of a discrete parcel of working fluid.

INTRODUCTION

A number of earlier investigations have developed modeling methods for thermal storage [1–5]. Earlier analyses of phase change thermal storage have generally modeled specific details of heat transfer in the storage unit structure. Most are either strictly analytical, numerical, or experimental. Alkilani et. al conducted a theoretical investigation of output air temperature of an indoor heater which utilizes a PCM heat exchanger [4]. Tay et. al used an ε-NTU method to generate an analytical solution to track latent heat transfer in a thermal storage device [5]. Ismail and Goncalves explored a two-dimensional model of a tube immersed in PCM [3]. By defining an appropriate control volume, the authors employ a finite difference scheme

to characterize how the TES melt fraction, number of transfer units (NTU), and effectiveness are dependent on various parameters. Others combine analysis with computational research techniques, though few have experimental data available with which they validate their work. For example, Shamsundar et. al look at a three-dimensional shell and tube configuration both analytically and numerically (via finite difference) in which the working fluid temperature changes axially as heat is transferred from the PCM [1]. As is clear from these papers, there is a need for experimental comparison that validates the many closed form solutions as well as computational results that researchers have generated.

The methodology and results that are presented in this paper are built upon a larger body of work from this group over the last several years [6–10]. The first of these contains the derivation of a non-dimensional framework developed in order to analyze thermal energy storage technology [6]. From there, efforts were focused on quantifying the space and time varying conductance inherent in the transient melting and freezing processes of latent thermal storage. That work was used to justify the use of an average conductance in future modeling; the effectiveness of high performance devices is not sensitive to variations in conductance [7]. Additional work has been done since then to determine a simpler relation for average conductance as a function of the melt fraction [8]. In tandem, the TES device was examined in the context of a larger subsystem, consisting of external heat exchangers used to input and reject heat to and from the storage. This problem was mathematically challenging by introducing spatially varying initial conditions (due to the nature of cyclic melting and freezing processes) as well as a transient boundary condition (for the varying working fluid temperature from the heat exchangers) [9]. The system equations derived in this paper were applied to model the performance of a power plant using TES for asynchronous cooling of a Rankine cycle steam condenser [10]. This paper demonstrated the economic viability of thermal storage and all that remains is to validate the numerical framework used in previous explorations.

In earlier studies, there is little to no experimental data with which to validate numerical models. The culmination of previous work provides a great basis for comparison with experimental testing of a TES device. Thus, the primary objective of this paper is to compare recent modeling to new experimental data.

METHODOLOGY

Three differential equations govern the temperature and melt fraction fields within a thermal energy storage device. Thermal energy is advected by the working fluid and enters or leaves the storage matrix through the channel wall.

$$\frac{\partial T_w}{\partial t} = -\left(\frac{\dot{m}}{\rho_w A_c}\right)\frac{\partial T_w}{\partial z} + \frac{U s_w}{\rho_w A_c c_{p,w}}(T_e - T_w) \tag{1}$$

$$\frac{\partial T_e}{\partial t} = \frac{U s_w}{\rho_s c_{p,s} v'}(T_w - T_e) \quad ; \quad \frac{\partial x_e}{\partial t} = 0 \tag{2}$$

for $T_e \neq T_m$ (sensible heat transfer) and $x_e = 0$ or $x_e = 1$.

$$\frac{\partial x_e}{\partial t} = \frac{U s_w}{\rho_s h_{ls} v'}(T_w - T_e) \quad ; \quad \frac{\partial T_e}{\partial t} = 0 \tag{3}$$

for $T_e = T_m$ (latent heat transfer) and $0 < x_e < 1$.

These equations are converted to a non-dimensional framework, as is typically done for heat exchanger analysis (e.g. effectiveness-NTU). Due to the complex nature of phase change physics, we require several dimensionless groups to predict performance. The differential equations within the TES device are non-dimensionalized using the following definitions:

$$\theta = \frac{T_e - T_{min}}{T_{max} - T_{min}} \quad , \quad \phi = \frac{T_w - T_{min}}{T_{max} - T_{min}} \tag{4}$$

$$\hat{z} = \frac{z}{L} \quad , \quad t^* = \frac{t}{t_{res}} \quad , \quad t_{res} = \frac{\rho_w A_c L}{\dot{m}} \tag{5}$$

These non-dimensional equations scale ϕ, θ, and x_e such that each of these variables takes on values between 0 and 1.

$$\frac{\partial \phi}{\partial t^*} = -\frac{\partial \phi}{\partial \hat{z}} + \mathrm{N_{tu}}(\theta - \phi) \tag{6}$$

$$\frac{\partial \theta}{\partial t^*} = \mathrm{N_{tu}R_{we}}(\phi - \theta) \quad ; \quad \frac{\partial x_e}{\partial t^*} = 0 \tag{7}$$

for $\theta \neq \theta_m$ and $x_e = 0$ or $x_e = 1$.

$$\frac{\partial x_e}{\partial t^*} = \mathrm{N_{tu}R_{we}St_{io}}(\phi - \theta) \quad ; \quad \frac{\partial \theta}{\partial t^*} = 0 \tag{8}$$

for $\theta = \theta_m$ and $0 < x_e < 1$.

Relevant dimensionless parameters are formed to concisely write the governing equations. Two of the non-dimensional groups are similar to those that result from compact heat exchanger analysis, with the addition of a third that accounts for latent heat transfer. The number of transfer units, $\mathrm{N_{tu}}$, relates the heat transfer into the matrix to that advected along the flow. It is critical for design because it encapsulates the conductance, UA, which is inherently dependent on the device configuration. The second parameter, $\mathrm{R_{we}}$, is the ratio of thermal capacities between the working fluid and matrix element and thus is dependent on the materials selected. The third parameter, the Stefan number,

$\mathrm{St_{io}}$, relates the relative importance of sensible heat transfer to latent heat transfer. This captures the operating conditions, namely the temperature range in which the thermal energy storage is used. For the previously outlined purpose to transfer energy via latent heat transfer, the Stefan number will be quite small. These dimensionless groups are defined as:

$$\mathrm{N_{tu}} = \frac{U s_w L}{\dot{m} c_{p,w}}, \quad \mathrm{R_{we}} = \frac{\rho_w c_{p,w} A_c}{\rho_s c_{p,s} \nu'}, \quad \mathrm{St_{io}} = \frac{c_{p,s}(T_{max} - T_{min})}{h_{ls}} \tag{9}$$

Typical values of the dimensionless numbers for the energy applications considered here might be:

$$\mathrm{N_{tu}} = \mathscr{O}(10^1), \quad \mathrm{R_{we}} = \mathscr{O}(10^0), \quad \mathrm{St_{io}} = \mathscr{O}(10^{-1}) \tag{10}$$

These will be calculated from TES device geometry, thermophysical properties, and transport parameters.

Numerical Framework

In order to solve the differential equations numerically, we use a first order accurate finite difference approximation, employing the upwind and forward Euler discretization methods respectively. The temperature and melt fraction fields in the storage matrix are determined using these equations. This working fluid temperature, ϕ, is dictated by:

$$\phi_j^{n+1} = \phi_j^n + \Delta t^* \left[\mathrm{N_{tu}} (\theta_j^n - \phi_j^n) \right] - \frac{\Delta t^*}{\Delta \hat{z}} \left[\phi_j^n - \phi_{j-1}^n \right] \tag{11}$$

This equation is first order in time and space, necessitating a boundary and an initial condition. The working fluid exchanges heat with phase change material in the storage matrix which undergoes both sensible and latent heat transfer depending on the temperature of each discrete node. Sensible energy storage occurs when a cell containing PCM at position $j\Delta\hat{z}$ and time $n\Delta t^*$ is not at its melt temperature, θ_m. The storage matrix temperature at the next time step can be determined via:

$$\theta_j^{n+1} = \theta_j^n + \Delta t^* \left[\mathrm{N_{tu}} \mathrm{R_{we}} (\phi_j^n - \theta_j^n) \right] \quad ; \quad x_{e,j}^{n+1} = x_{e,j}^n \tag{12}$$
$$\text{for } \theta_j^n \neq \theta_m \text{ and } x_{e,j}^n = 0 \text{ or } x_{e,j}^n = 1.$$

If Eqn. 12 would result in the temperature at the next time step, $n+1$, to pass the melt temperature, then θ_j^{n+1} is set to θ_m and latent energy storage begins, with change in melt fraction calculated from Eqn. 13:

$$x_{e,j}^{n+1} = x_{e,j}^n + \Delta t^* \left[\mathrm{N_{tu}} \mathrm{R_{we}} \mathrm{St_{io}} (\phi_j^n - \theta_j^n) \right] \quad ; \quad \theta_j^{n+1} = \theta_j^n \tag{13}$$
$$\text{for } \theta_j^n = \theta_m \text{ and } 0 < x_{e,j}^n < 1.$$

The equations governing the storage matrix temperature and melt fraction are first order in time but have no spatial derivative. As such, only one boundary condition is required to solve these coupled first order differential equations. In $\hat{z}$, we nondimensionalize the time varying working fluid inlet temperature, T_{wi}, to write the boundary condition in its dimensionless form:

$$\text{At } \hat{z} = 0: \quad \phi_{j=1}^n = \phi_{wi}(t^*) \tag{14}$$
$$\text{for } t^* > 0.$$

Initial conditions on temperatures, ϕ and θ, and melt fraction, x_e, are also required for the entire domain. At the beginning of extraction, we might expect the PCM in the device to be completely frozen at the cold system temperature, corresponding to dimensionless values of 0 for ϕ, θ, and x_e. Conversely, after a complete melting process ending at the hot system temperature, the initial conditions for re-freezing the device might correspond to dimensionless values of 1. That said, these can represent any distribution desired as in Eqn. 15:

$$\text{At } t^* = 0: \quad \phi_j^{n=1} = \phi_0(\hat{z}) \, , \; \theta_j^{n=1} = \theta_0(\hat{z}) \, , \; x_{e,j}^{n=1} = x_{e,0}(\hat{z}) \tag{15}$$
$$\text{for } 0 \leq \hat{z} \leq 1.$$

These initial and boundary conditions can be spatially uniform and temporally steady. To capture physical complexity, the initial conditions can be modified to match the end and beginning of subsequent processes; the boundary condition can be adjusted to capture time-varying conditions. The temperature and melt fraction fields should be resolved spatially and temporally until the melting or freezing process end time, t_{end}^*, is reached. In order to determine device performance at t_{end}^*, the following equation should be used to evaluate effectiveness, ε_{tes}:

$$\varepsilon_{tes,ext} = \frac{\sum_{\hat{z}=0}^{1} x_e(t_{end}^*, \hat{z})}{\sum_{\hat{z}=0}^{1} x_{e,max}(t^*, \hat{z})} \quad \text{where} \quad x_{e,max} = 1 \tag{16}$$
$$\text{for the extraction (melting) process.}$$

$$\varepsilon_{tes,char} = \frac{\sum_{\hat{z}=0}^{1} 1 - x_e(t_{end}^*, \hat{z})}{\sum_{\hat{z}=0}^{1} 1 - x_{e,min}(t^*, \hat{z})} \quad \text{where} \quad x_{e,min} = 0 \tag{17}$$
$$\text{for the charging (freezing) process.}$$

The storage process, which may occur between extraction and charging processes, is not characterized as having an effectiveness (because no energy is added or removed from the device). For the experimental testing of the prototype described in subsequent sections, charging immediately followed extraction; no storage took place. The effectiveness for either extraction or

charging has the functional relationship:

$$\varepsilon_{tes} = \varepsilon_{tes}(t^*, \mathrm{N_{tu}}, \mathrm{R_{we}}, \mathrm{St_{io}}) \tag{18}$$

In addition, the energy capacity of the TES can be calculated according to:

$$E_{cap} = \rho_{PCM} v' L h_{ls} \varepsilon_{tes} \tag{19}$$

EXPERIMENT DESIGN

The remainder of this paper is dedicated to applying the methodology and numerical framework described above to a 100 kJ TES device. A compact heat exchanger (CHX) was fabricated and assembled by a commercial vendor (Allcomp Inc.) and subsequently filled with a phase change material. The working fluid, i.e. the heat transfer fluid (HTF), was used to melt and solidify the PCM in repeated thermal cycles involving complete solidification and incomplete melting; this technique is called the "cold finger" approach. The TES has an offset fin configuration on the working fluid side and aluminum porous fins in the storage matrix. The device has five flow channels for HTF flow and four hermetically sealed channels with encapsulated PCM. Experimental testing of this prototype was performed at Texas A&M.

Device Geometry

The TES prototype consists of stacked rectangular sections, alternating between flow passages and storage matrix sections. The unit was fabricated using mature fin forming and vacuum brazing processes. The liquid-side heat transfer surface is a 3000 series aluminum offset fin, while the PCM-side utilizes a high density plain fin formed from 5056-O aluminum wire mesh. The TES HX core is comprised of four PCM cavities that are sandwiched between five liquid cooling passages. Header caps were bonded to the TES HX core to support cyclic testing. Note that the assembly of a mass produced TES unit would employ a more robust joining technique (e.g. welding).

TABLE 1: Thermal Energy Storage Prototype Geometry.

Length of TES device, L	0.407	m
Wetted perimeter of flow passage, s_w	$9.42 * 10^{-2}$	m
Cross sectional area of flow passage, A_c	$8.97 * 10^{-5}$	m^2
Matrix volume per unit flow length, v'	$1.99 * 10^{-4}$	m^2
Number of flow passages, n_w	5	
Number of storage matrix sections, n_s	4	
Void fraction in storage matrix, ε_s	0.729	

The HTF region of the TES had an offset fin density of 22 fins per inch; the offset fin configuration was selected due to its high surface area. The heat exchanger and offset fins were manufactured using Al-3003 material. The PCM channels are brazed with aluminum foam (porous fin). The aluminum porous fin was formed by folding a porous aluminum thread (wire) based fabric sheet. The purpose of the aluminum foam is to enhance the effective thermal conductivity of PCM.

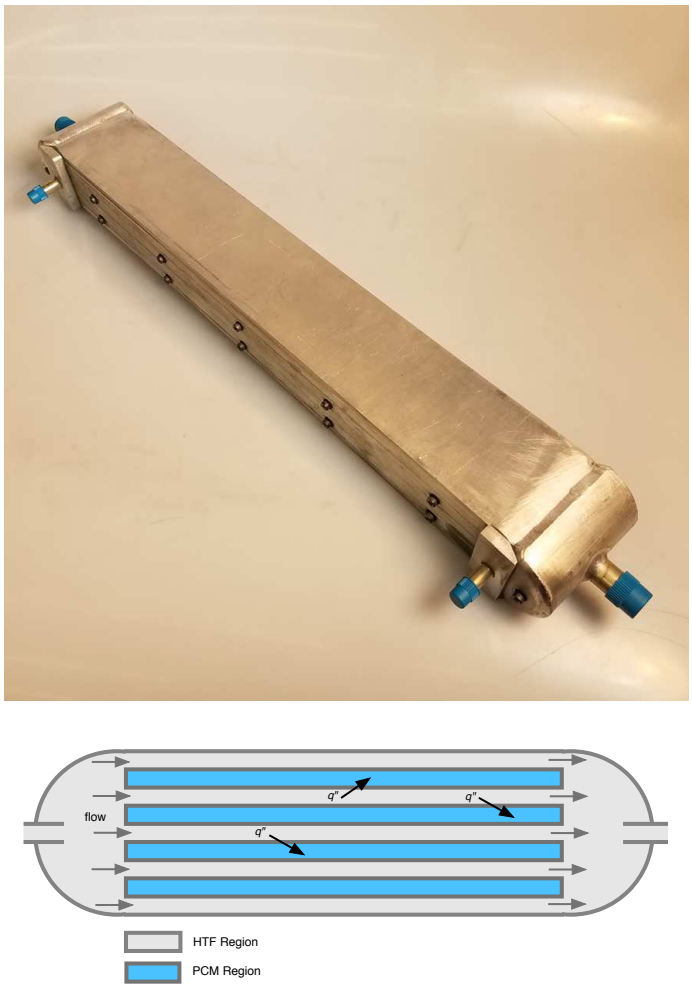

FIGURE 1: Photograph and schematic (not to scale) illustrating heat flux (q'') from hot HTF region into PCM region during melting process.

The design allowed the center PCM channels to have higher effective heat transfer area compared to top and bottom PCM channels as illustrated in Figure 1. This resulted in faster charging and discharging in the center PCM channels in comparison to the top and bottom PCM channels.

Specific details of the design are summarized in Table 1. Of

particular interest is the void fraction which greatly impacts the effective properties that form the dimensionless parameters in the governing equations.

Thermophysical Properties

There are four types of phase change materials that might be used in this type of application: organic paraffins, organic non-paraffins, inorganic salt hydrates, and inorganic metal eutectics [11]. Organic paraffins have a high latent heat of fusion but are derived from petroleum. Organic non-paraffins are not derived from petroleum but tend to be very expensive. Inorganic salt hydrates are very cheap but but unfortunately are unstable over repeated cycling. All of the above suffer from low thermal conductivity which makes the process of inputting or removing energy from the PCM more difficult. This can be remedied with an inorganic metal eutectic which has excellent thermal conductivity but a lower latent heat of fusion than other materials. When selecting an appropriate PCM among these, affordability is highly important. With all of these factors in mind, the material chosen for the prototype was lithium nitrate trihydrate, a salt hydrate that has been optimized to better handle transient cycling. Anhydrous lithium nitrate salt powders were procured commercially from Beantown Chemical, NH with purity greater than 99%. Thermophysical properties are shown in Table 2 [12].

TABLE 2: PCM Properties: Lithium Nitrate Trihydrate.

thermal conductivity, k_{PCM}	0.584	W/mK
density, ρ_{PCM}	1500	kg/m^3
specific heat, $c_{p,PCM}$	2910	J/kgK
latent heat of fusion, h_{ls}	278	kJ/kg
melting temperature, T_m	30	°C

Note: The melt temperature experimentally deviates from this single value, T_m, due to the subcooling or superheating required to initiate phase change.

The amount of PCM inserted into the TES was 474 grams. The filling rate of PCM does not affect the calculation nor the experimental results. Instead, we are concerned with the energy capacity of the PCM contained within the TES. The latent heat of LNT was measured in this study to be 278 kJ/kg using the T-History method. Thus, the theoretical energy storage capacity of the device was rated to be 130 kJ which differs slightly from the rated capacity of 100 kJ.

Other properties that are not solely associated with latent heat transfer can be adjusted by adding a metal mesh to the storage matrix. As the thermal conductivity of lithium nitrate trihydate is quite low, a metal matrix structure is required to effectively conduct heat through the storage matrix. Any high conductivity material would be suited for this application, but the low cost of aluminum makes it ideal for this technology. Its properties are shown in Table 3.

TABLE 3: Metal Mesh Properties: Aluminum 5056.

thermal conductivity, k_m	117	W/mK
density, ρ_m	2640	kg/m^3
specific heat, $c_{p,m}$	910	J/kgK

Aluminum is an cheap option that is chemically compatible with the PCM. Metal pathways are ideal for spreading the thermal energy away from the channel wall towards the melt front. They enhance the effective properties (conductivity, density, specific heat) of the storage matrix which are calculated according to:

$$\bar{p} = p_m(1-\varepsilon_s) + p_{pcm}\varepsilon_s; \tag{20}$$

The effective properties determined from Eqn. 20 are summarized in Table 4.

TABLE 4: Effective Properties: Storage Matrix.

effective thermal conductivity, k_s	32.1	W/mK
effective density, ρ_s	1810	kg/m^3
effective specific heat, $c_{p,s}$	2370	J/kgK

The thermophysical properties of the working fluid are also necessary in order to solve the governing equations. The experiments were conducted with pure de-ionized water. Its properties were taken at the inlet temperatures for extraction and for charging respectively. The ranges in Table 5 reflect the values associated with the cold and hot fluid inlet temperatures.

TABLE 5: Working Fluid Properties: Water.

thermal conductivity, k_w	0.608 - 0.623	W/mK
density, ρ_w	994 - 997	kg/m^3
specific heat, $c_{p,w}$	4090 - 4130	J/kgK

Experimental Apparatus and Procedure

The melt front and freeze front of the PCM in the top and center channels were monitored by embedding thermocouples

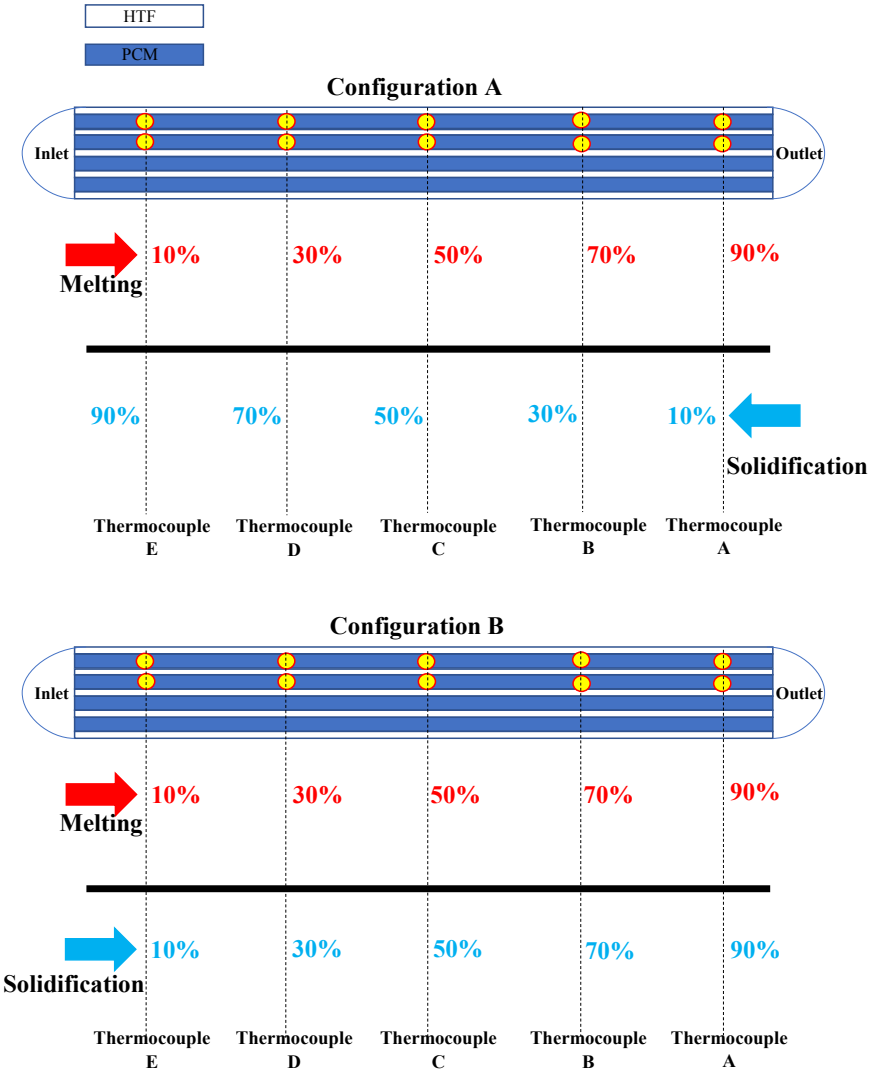

FIGURE 2: Schematic showing the location of thermocouples inserted in the CHX to monitor temperature during charging and extraction for two different flow configurations.

at predefined locations. The predefined locations correspond to 10%, 30%, 50%, 70%, and 90% melt fractions along the axial directions as illustrated in Figure 2. The temperature of the HTF was measured at the inlet and outlet plenum of the compact heat exchanger.

Two different HTF flow configurations (A and B) were explored during solidification and melting experiments to study the efficacy of cold finger techniques. Cold finger techniques involve thermal cycling protocols with complete solidification and incomplete melting of the PCM samples under consideration. The incomplete melting protocols enable a residue of PCM crystals to remain in the PCM sample - which in-turn act as nucleators by promoting nucleation. Prior studies have shown that having an un-melted portion of the PCM, like residue crystals, provides better efficacy for promoting nucleation than that of heterogeneous additives for the same purpose. The result is that freezing can initiate with subcooling less than 1 °C.

To realize the full effectiveness of the cold finger techniques, the experiments were designed for the flow of HTF in to the CHX to be bi-directional. In configuration A, the flow of HTF during melting is from left to right, whereas during solidification the flow of HTF was reversed to flow from right to left (i.e. opposite direction during charging and discharging). In configuration B, the flow of HTF during melting and solidification is from left to right (i.e. same direction during charging and discharging). For the complete melting and freezing tests, the flow direction matched configuration B, with both HTF flows in the same direction as shown in Fig. 2.

The cold finger experiments were designed for the melting to proceed until 90% of the total latent heat (i.e., the total energy storage capacity) was utilized, thus allowing about 10% of the remaining PCM to be un-melted and remain in solid phase as dispersed crystals or unused energy storage capacity. Thus, storage capacity is sacrificed marginally to enable more reliable operation by enhancing the efficacy of the residual crystals (unmelted portion of the PCM) to initiate the nucleation and subsequent propagation of the solidification front in the melted phase of the PCM. The variation in flow direction was manipulated with three-way valves with different valve configuration for melting and solidification.

The top PCM channel was used as the reference for monitoring the propagation of the melting front. The PCM charging and discharging temperature conditions were achieved using two different water baths. The hot water bath was maintained slightly above phase transition temperature (i.e., 35 °C) using a chiller unit and the cold water bath was maintained at a temperature below phase transition temperature (i.e., 25 °C). The two water baths (chiller units) were purchased from Cole-Parmer (Model: Polystat cooling/heating circulating baths, 2C15). Data was collected to indicate when 90% of the PCM was melted by hot HTF pumped into the TES from the hot water bath. At that point, the valves were switched to pumping of cooling HTF (freezing) from the cold water bath. At this switch point, the PCM matrix section temperature recorded by the thermocouple at the 90% melt fraction location of top channel reached 30.5 °C. This allowed for maximization of the storage capacity and enabled the implementation of the cold finger technique.

The thermocouples utilized in the temperature measurements were K-Type (1/16" diameter) with hydro-thermic sheathed tips (Sheathing Material: SS 316, and Manufacturer: Temprel, Ohio). The tip of the thermocouple is located centrally along the width of the heat exchanger (1.5" from the edge). The thermocouples were calibrated in a water bath from 10 °C to 40 °C at an interval of 0.5 °C using an NIST Standard thermometer (least count: ± 0.25 °C and calibration uncertainty of 0.8%). After calibration, the uncertainty of the thermocouples was determined to be ±0.25 °C to ±0.35 °C.

A high-speed data acquisition (DAQ) system was used for recording the temperature measured by the thermocouples. The DAQ consists of an NI SCXI 1000 Chassis and an NI SCXI-1303 board. The temperature measurements were performed at 1 Hz frequency (i.e. 1 reading/second). The least count accuracy of DAQ system was 0.003 °C; therefore, the uncertainty from the DAQ can be considered negligible. Simultaneously, the voltage measurement from the flow meter was acquired using an NI USB 9162 DAQ at 1 Hz frequency. The HTF volumetric flow rate in the system was measured by an Omega FLR 1000 series flow meter (S/N 10981) which was calibrated for 0.2 L/min to 2 L/min (purchased from OMEGA).

The efficacy of cold finger techniques was experimentally validated in this TES. To summarize, the cold finger protocol consisted of 90% melting of PCM — leaving 10% of PCM as solid crystals prior to complete solidification of PCM. The flow direction of the HTF was varied to study the sensitivity of flow direction on solidification and the sub-cooling required to initiate freezing.

The thermal performance of the TES was analyzed by varying (a) the flow rate of the HTF during charging and discharging, and (b) the inlet temperature of the HTF during charging and discharging. The volumetric flowrate was varied between 3 and 5 gallons per hour and the HTF inlet temperatures tested during melting were 33 °C, 35 °C, and 37.4 °C. Similarly, during solidification, the HTF inlet temperature was varied between 20 °C and 25 °C. The design condition for the compact heat exchanger was 3 gallons per hour with inlet temperature of 37.4 °C during melting (discharging) and 25 °C during freezing (charging). The experiments were repeated two times with and without insulation to ensuring repeatability of the experiments. The insulated and un-insulated cases allowed for comparison of parasitic heat loss to the environment during the melting and solidification process.

The experimental steps are listed as follows:

1. Initially solidify PCM with HTF at cold inlet temperature.
2. Close the cold HTF control valve and turn valves to direct the hot HTF.
3. Open the hot HTF control valve and melt to the 90% mass fraction of un-melted PCM.
4. Close the hot HTF flow control valve and turn valves to direct the cold HTF.
5. Completely solidify the PCM.
6. Repeat steps (2) through (5) above for ensuring repeatability and for varying HTF mass flowrate and inlet temperature.

The temperature difference of the HTF between inlet and outlet was computed as follows:

$$\Delta T_{HTF} = T_{outlet} - T_{inlet} \tag{21}$$

where T_{outlet} is the HTF temperature measured at the outlet port of the heat exchanger and T_{inlet} is the inlet temperature measured at the inlet port of the heat exchanger. The measurement uncertainty of the ΔT_{HTF} was estimated by using the following equation:

$$u_{\Delta T} = \left[\left(\frac{\partial \Delta T_{HTF}}{\partial T_{outlet}} \right)^2 (u_{T_{out}})^2 + \left(\frac{\partial \Delta T_{HTF}}{\partial T_{inlet}} \right)^2 (u_{T_{in}})^2 \right]^{1/2} \tag{22}$$

where u is the statistical uncertainty for each variable. The calibrated uncertainty of thermocouples was determined to be ± 0.35 °C between 10 °C and 40 °C. The nominal value for the measurement uncertainty for ΔT_{HTF} is therefore estimated to be

$\pm$ 0.49 °C. The experimental effectiveness (ε) of the TES was determined using the following equation:

$$\varepsilon = \frac{T_{inlet} - T_{outlet}}{T_{inlet} - T_{PCM}} \tag{23}$$

where T_{PCM} is the local temperature of the of the PCM. The thermal storage capacity of the heat exchanger at any instant was calculated by using Equation 24, based on the measurements of the HTF temperature values and mass flow rates:

$$E = m_w c_{p,w} \Delta T_{HTF} \tag{24}$$

where m_w is the total mass flow over a short duration of the experiment and $c_{p,w}$ is the specific heat capacity of the HTF. The cumulative values of the instantaneous thermal energy storage can be used to estimate the total energy storage capacity of the TES for either the charging or discharging portion of the cycle. The instantaneous power, P, for the TES was calculated as follows:

$$P = \dot{m}_w c_{p,w} \Delta T_{HTF} \tag{25}$$

where $\dot{m}_w$ is the mass flow rate at any instant. The instantaneous power can be integrated over a specified time period and divided by the total time period in order to obtain the average power over the chosen time period. The Stefan number (St) at any instant can be estimated using the following equation:

$$\text{St} = \frac{(\text{Sensible Heat})}{(\text{Latent Heat})} = \frac{c_{p,w} \Delta T_{HTF}}{h_{ls}} \tag{26}$$

where h_{ls} is the latent heat of fusion of the phase change material.

Model Transport Parameters

The total flow rates for extraction and charging were provided with TAMU experimental data. Due to a 4.3 % uncertainty reported in flow rate measurements, a slightly lower flow rate was input into the numerical model to account for any hydrodynamic losses. The total mass flow rate, given in Table 6, is assumed to be distributed equally among the 5 flow passages in the device.

TABLE 6: Thermal Energy Storage Operating Parameters.

Mass flow rate for extraction, $\dot{m}_{ext}$	$3.44 * 10^{-3}$	kg/s
Mass flow rate for charging, $\dot{m}_{char}$	$3.56 * 10^{-3}$	kg/s
Inlet temperature for extraction, $T_{wi,ext}$	36	°C
Inlet temperature for charging, $T_{wi,char}$	26	°C

The working fluid in all tests came in at a relatively constant inlet temperature after being ramped up or down to that, respectively. The properties of the working fluid were assumed to be constant throughout a given process and determined based on the average water inlet temperature.

Calculating Conductance With the device geometry, thermophysical properties, and transport parameters specified, a convective heat transfer coefficient can be determined via correlation. The flow passages consist of offset fins, giving a Colburn-j type relation:

$$j = .6522 * \text{Re}^{-.5403} \left(\frac{s}{h_f}\right)^{-.1541} \left(\frac{t_f}{l_f}\right)^{.1499} \left(\frac{t_f}{s}\right)^{-.0678} \left(1 + 5.269 * 10^{-5} \text{Re}^{1.340} \left(\frac{s}{h_f}\right)^{.504} \left(\frac{t_f}{l_f}\right)^{.456} \left(\frac{t_f}{s}\right)^{-1.055}\right)^{-.1} \tag{27}$$

where Re is the Reynolds number of the flow, s is the spacing between fins, h_f is the height of the fins, t_f is the thickness of the fins, and l_f is the length of the fins.

The Colburn-j factor is used to calculate the Stanton number, which is subsequently used to calculate the Nusselt number, and from there, solve for the convective heat transfer coefficient, h:

$$\text{St} = \frac{j}{\text{Pr}^{2/3}}$$

$$\text{Nu} = \text{StRePr} \tag{28}$$

$$h = \frac{k_w \text{Nu}}{D_h}$$

With h, the overall heat transfer coefficient, U, can be found. Based on geometry, a stability analysis is performed for the PCM matrix enclosure to determine whether or not natural convection occurs. A fluid heated from the bottom is stable provided its Rayleigh number is below a critical value. The Rayleigh number has a cubic dependence on the characteristic length. For the geometry given in Table 1, natural convection is not present. As noted in the introduction, previous work has been used to derive U [7, 8]. The more elegant of these results will be used, namely that the overall heat transfer coefficient, U, can be found from the device geometry (A_t, A_w, h_s), thermophysical properties (k_s), convective coefficient, h, and the melt fraction, x_e, which is a function of position in the device as well as time:

$$U_{ext} = \left[\frac{1}{h(A_t/A_w)} + \frac{h_s}{2k_s} x_e\right]^{-1} \tag{29}$$

where $A_t/A_w = (\eta_{\text{fin}} h_f + s)/(s + t_f)$ including the offset fin efficiency and h_s is the height of the storage matrix sections.

A key finding from both studies of conductance was that an average U could be used in place of a spatially and temporally varying one. To be sure that this was also the case for the prototype experiments, we applied a quasi-steady treatment of the variation of U with x_e and compared our results to constant conductance. As the conductance is quite high, we see no measurable difference in the fluid outlet temperature predicted. Thus, an average conductance is suitable for modelling the TES. In order to average Eqn. 29, we integrate over the range of x_e encountered during the melting process.

$$\bar{U}_{ext} = \frac{1}{x_{e,f}} \int_{x_{e,i}=0}^{x_{e,f}=1} \left[\frac{1}{h(A_t/A_w)} + \frac{h_s}{2k_s} x_e \right]^{-1} dx_e \qquad (30)$$

After integrating over melt fraction and normalizing by the final value, we find that:

$$\bar{U}_{ext} = \frac{2k_s}{h_s} \ln \left[1 + \frac{h_s}{2k_s} h(A_t/A_w) \right] \qquad (31)$$

This gives a value for $\bar{U}_{ext}$ that falls between the convective heat transfer coefficient (h) and the steady state value reached at the end of melting that U asymptotes to when the PCM melt front reaches the adiabat between flow passages. The key term in the variable U expression, x_e, can be interpreted as a proxy for the growing distance between the channel wall and the melt front. This term is the dominant thermal resistance in the problem due to the high efficiency of the working fluid side heat transfer. By extrapolating this simple model to freezing, we predict the values given in Table 7 for TES conductance.

TABLE 7: Averaged Overall Heat Transfer Coefficient, $\bar{U}$.

Run 1 Ext	2990	W/m^2K
Run 1 Char	2880	W/m^2K
Run 2 Ext	2980	W/m^2K
Run 2 Char	2930	W/m^2K

This average overall heat transfer coefficient is subsequently used to calculate N_{tu}, the number of transfer units, required to solve the non-dimensionalized set of equations that comprise the numerical framework. The complete set of parameters in the three governing equations would be non-dimensionalized according to Eqn. 9 giving the values in Table 8.

TABLE 8: Thermal Energy Storage Dimensionless Variables.

	N_{tu}	R_{we}	St_{io}
Run 1 Ext	32.4	0.534	0.234
Run 1 Char	31.2	0.541	0.234
Run 2 Ext	32.5	0.534	0.234
Run 2 Char	30.4	0.541	0.234

RESULTS AND DISCUSSION

Table 8 enables us to proceed with the solution of the differential Eqns. 11, 12, and 13 with boundary condition given by Eqn. 14 and initial conditions from Eqn. 15. The boundary condition is a time varying working fluid inlet temperature, shown in red in Figures 3, 4, and 5. The initial condition is taken to be completely frozen at the start of melting (0 min) while the spatial distribution at the end of extraction ($\sim$ 34 min) serves as the initial condition for the freezing process. Solving the differential equations with these conditions provides spatially and temporally resolved temperature and melt fraction fields. The grid size used to solve the equations for the results presented in this paper are $\Delta\hat{z} = .005$ and $\Delta t^* = .00025$.

TABLE 9: Time to Complete Processes: Run 1.

Experimental melting completed:	27.0	min
Numerical melting completed:	25.8	min
Percent difference	**4.42**	%
Experimental freezing completed:	85.2	min
Numerical freezing completed:	76.5	min
Percent difference	**10.7**	%

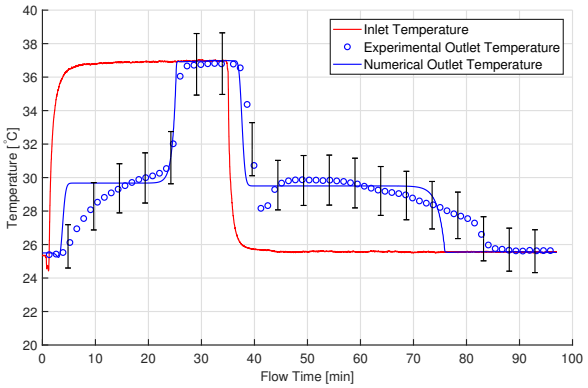

FIGURE 3: Complete Melting and Freezing: Run 1.

Note: For extraction, the melt temperature was taken to be

29.66°C and for charging, the melt temperature was taken to be 29.5°C. These values are well within the range predicted by experiments.

Four experimental tests were conducted at TAMU. Two of these consisted of complete melting and freezing while the others examined incomplete melting followed by freezing. This was done in an effort to combat the poor nucleation rates that resulted once the entire PCM domain was liquid. While all four tests are important, those with complete melting and freezing are most relevant for comparison to the numerical model. The metric used to determine whether or not the numerics effectively captures the physics is the process end time (e.g. time to melt, time to freeze). For Runs 1 and 2, the completion times summarized in Tables 9 and 10 were observed.

Run 2, with transient inlet and outlet temperatures reproduced in Fig. 4, generated similar results to Run 1 shown in Fig. 3. Both of these figures present the comparison of experimental and numerical inlet and outlet temperature measurements. The error bars depict experimental uncertainty and serve to highlight just how well the simulation predicts the results.

TABLE 10: Time to Complete Processes: Run 2.

Experimental melting completed:	26.5	min
Numerical melting completed:	25.5	min
Percent difference	**3.85**	%
Experimental freezing completed:	89.5	min
Numerical freezing completed:	74.8	min
Percent difference	**17.8**	%

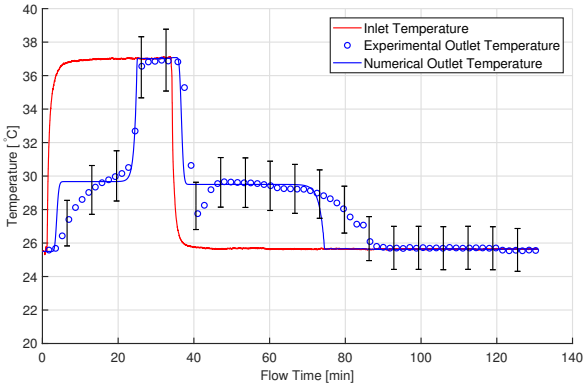

FIGURE 4: Complete Melting and Freezing: Run 2.

It is challenging to capture the exact heat transfer physics with the computational program. This is evidenced by disagreement between the curves below the melt temperature for both extraction and charging. However, this disagreement falls mostly within the 5 % uncertainty associated with temperatures measured in the experiment. Where the numerical prediction does not fall within error bars, the absolute difference between experimental measurement and numerical prediction is around one to two degrees Celsius. This lends significant support to the accuracy of the model prediction. Even more importantly, the process completion time is quite close, ranging between 4 and 18 % difference.

The highest discrepancy is observed during freezing. There, the numerical program is not designed to capture the poor nucleation rates that necessitate subcooling (at $\sim$ 40 minutes) before the phase change material can start freezing.

Due to the accuracy with which the computational model can be used to predict process completion times, it can be used as a highly efficient and cheap design tool. For example, the number of fins per inch within the storage matrix sections can be reduced, thereby increasing the void fraction, and decreasing the overall heat transfer coefficient. To maintain a consistent amount of energy storage capacity, the height of the storage matrix sections can be reduced, resulting in the same amount of PCM in the TES device. The conductance associated with this proposed design is enumerated in Table 11.

TABLE 11: Overall Heat Transfer Coefficient, $\bar{U}$.

	25 fins/inch	100 fins/inch	
Run 1 Extraction	2520	2990	W/m^2K
Run 1 Charging	2440	2880	W/m^2K

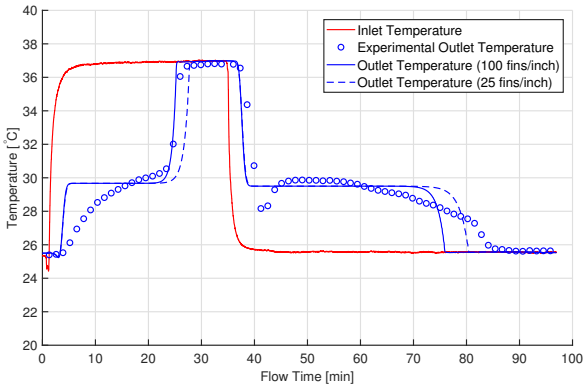

FIGURE 5: Complete Melting and Freezing: Run 1 with slight design modifications.

The result of this reduction in metal in the storage matrix is shown here. As evidenced by Fig. 5, the melting and extraction processes take only slightly longer than their 100 fins/inch

counterpart prediction. This indicates that a cheaper design, using 1/4 of the metal in the storage matrix, would still produce a TES device that performs within the desired time.

CONCLUSIONS

The work discussed in this paper demonstrates experimental validation of performance models for high-performance TES designs. We presented a summary of performance tests of a TES unit with lithium nitrate trihydrate phase change material as a storage medium. The experimental research included thorough property determinations and cyclic testing of the PCM. The presented performance data is for complete dual-mode cycles consisting of extraction and charging. The model analysis is found to agree very well with experiments, within 5% for melting and within 18% for freezing. Higher percent deviation with the experimental data is attributed to conditions very near the initiation of freezing. This is a consequence of subcooling that is required to initiate solidification. Given the success of the cold finger techniques discussed herein, we expect to eliminate these issues in subsequent comparisons. The work presented here demonstrates the viability of thermal energy storage for many latent heat TES applications. Moreover, this research is novel in its demonstration that spatial and temporal variation within a TES device can be effectively simulated and validated.

ACKNOWLEDGMENT

Thanks to the ARID program of ARPA-E for providing funding for this project. Our group would also like to acknowledge Dr. Jianping (Gene) Tu of Allcomp Inc. for design and fabrication of the 100 kJ TES device used in this study.

REFERENCES

[1] Shamsundar, N., and Srinivasan, R., 1980. "Effectiveness-ntu charts for heat recovery from latent heat storage units". *Journal of Solar Energy Engineering,* **102**(4), pp. 263–271.

[2] Bellecci, C., and Conti, M., 1993. "Transient behaviour analysis of a latent heat thermal storage module". *International Journal of Heat and Mass Transfer,* **36**(15), pp. 3851–3857.

[3] Ismail, K., and Goncalves, M., 1999. "Thermal performance of a pcm storage unit". *Energy Conversion and Management,* **40**(2), pp. 115–138.

[4] Alkilani, M., Sopian, K., Mat, S., and Alghoul, M., 2009. "Output air temperature prediction in a solar air heater integrated with phase change material". *European Journal of Scientific Research,* **27**(3), pp. 334–341.

[5] Tay, N., Belusko, M., and Bruno, F., 2012. "An effectiveness-ntu technique for characterising tube-in-tank phase change thermal energy storage systems". *Applied Energy,* **91**(1), pp. 309–319.

[6] Helmns, A., and Carey, V. P., 2016. "Modeling of heat transfer and energy efficiency performance of transient cold storage in phase change thermal storage components". In ASME 2016 Heat Transfer Summer Conference, American Society of Mechanical Engineers, pp. V001T05A009–V001T05A009.

[7] Helmns, A., and Carey, V. P., 2017. "Modeling of intra-matrix heat transfer in thermal energy storage for asynchronous cooling". In ASME 2017 Heat Transfer Summer Conference, American Society of Mechanical Engineers, pp. V001T09A006–V001T09A006.

[8] Theroff, Z. M., Helmns, D., and Carey, V. P., 2018. "Exploration of variable conductance effects during input and extraction of heat from phase change thermal storage". In ASME 2018 International Mechanical Engineering Congress and Exposition, American Society of Mechanical Engineers.

[9] Helmns, A., and Carey, V. P., 2018. "Multiscale transient modeling of latent energy storage for asynchronous cooling". *Journal of Thermal Science and Engineering Applications,* **10**(5), p. 051004.

[10] Gagnon, L. B., Helmns, D., and Carey, V. P., 2018. "Multiscale modeling of power plant performance enhancement using asynchronous thermal storage and heat rejection". In ASME 2018 International Mechanical Engineering Congress and Exposition, American Society of Mechanical Engineers.

[11] Kumar, N., and Banerjee, D., 2018. "Phase change materials". *Handbook of Thermal Science and Engineering*, pp. 2213–2275.

[12] Shamberger, P. J., and Reid, T., 2012. "Thermophysical properties of lithium nitrate trihydrate from (253 to 353) k". *Journal of Chemical & Engineering Data,* **57**(5), pp. 1404–1411.